Nanoelectronics and Its New Materials – A NEW ERA OF NANOSCIENCE
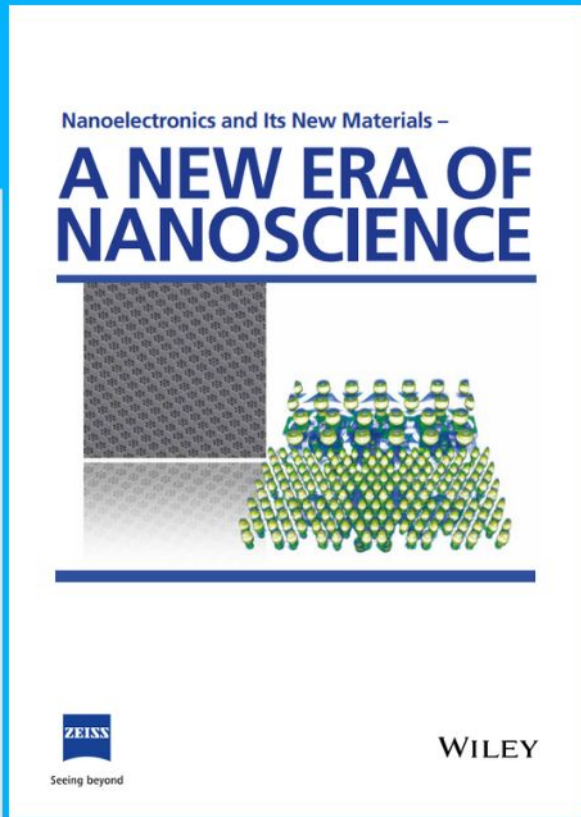
Discover the recent advances in electronics research and fundamental nanoscience.

Nanotechnology has become the driving force behind breakthroughs in engineering, materials science, physics, chemistry, and biological sciences. In this compendium, we delve into a wide range of novel applications that highlight recent advances in electronics research and fundamental nanoscience. From surface analysis and defect detection to tailored optical functionality and transparent nanowire electrodes, this eBook covers key topics that will revolutionize the future of electronics.

To get your hands on this valuable resource and unleash the power of nanotechnology, simply download the eBook now. Stay ahead of the curve and embrace the future of electronics with nanoscience as your guide.

Production of Metal-Free C, N Alternating Nanoplatelets and Their In Vivo Fluorescence Imaging Performance without Labeling

Dawoon Jang, Heesu Ahn, Junghoon Oh, Donggyu Lim, Chul Hee Kim, Seungjoo Choi, Young-Hoon Kim, Jinwoo Park, Kyeong Yeon Jang, Ran Ji Yoo, Tae-Woo Lee, Jeongho Kim, Yong Jin Lee,* Dong Wook Kim,* and Sungjin Park*

The use of luminescent probes with proper optical and morphological properties, high serum stability, low cytotoxicity, and good biocompatibility is a cost-effective method for bioimaging. In this work, a route is developed to produce a novel bioimaging probe framework. A C_3N_4 material (UCN-H) is produced by thermal condensation of urea under humidified air treatment. Chemical characterizations reveal that the UCN-H contains C_3N_4 networks with smaller grain sizes and more amine-based functionalities at the edges than UCN, which is separately produced without the humidified air treatment. Highly stable aqueous dispersions including fluorescent C_3N_4 nanoplatelets are generated by sonication of the UCN-H powder. The photoluminescence (PL), time resolved-PL, and 2D excitation-emission spectra of the dispersions show that the UCN-H has less-intra bandgap traps and longer PL lifetime than UCN. In confocal microscopic study using the nanoplatelets, clear fluorescent cell images are obtained without any cytosolic aggregation. In in vivo imaging studies with MDA-MB-231 tumor-bearing mice models, persistently strong fluorescence signals are successfully observed on tumor lesions without any interference of autofluorescence from live tissues after their accumulation by passive tumor targeting. Ex vivo biodistribution and histology results are well-matched with in vivo fluorescence imaging results.

1. Introduction

Visualizing cells in living organisms is an efficient method for early diagnosis and therapy of diseases, and image-guided surgery.[1–7] The use of luminescent probes has proven to be a possible cost-effective solution for this purpose. For practical applications, such probes need to show photoluminescence (PL) of visible light, stable dispersibility in cell media, biocompatibility, and low cytotoxicity. Recently, semiconducting nanomaterials such as quantum dots (QD) based on heavy metals have been suggested as candidates due to their suitable optical properties and nanoscale dimensions.[8–11] However, their application is restricted by high cytotoxicity of the metal-components and limited dispersibility. Consequently, it is highly important to develop new luminescent, metal-free nanomaterials with appropriate optical, morphological, and biological properties.

D. Jang, Dr. J. Oh, D. Lim, C. H. Kim, S. Choi, Prof. J. Kim,
Prof. D. W. Kim, Prof. S. Park
Department of Chemistry and Chemical Engineering
Inha University
100 Inha-ro, Michuhol-gu, Incheon 22212, Republic of Korea
E-mail: kimdw@inha.ac.kr; sungjinpark@inha.ac.kr
H. Ahn, Prof. Y. J. Lee
Division of Applied RI
Korea Institute of Radiological and Medical Sciences
75 Nowonro, Nowongu, Seoul 01812, Republic of Korea
E-mail: yjlee@kirams.re.kr
H. Ahn
Radiological and Medico-Oncological Sciences
University of Science and Technology
Daejeon 34113, Republic of Korea

Dr. Y.-H. Kim, J. Park, K. Y. Jang, Prof. T.-W. Lee
Department of Materials Science and Engineering
Seoul National University
1 Gwanak-ro, Gwanak-gu, Seoul 08826, Republic of Korea
Dr. R. J. Yoo
Korea Radioisotope Center for Pharmaceuticals
Korea Institute of Radiological and Medical Sciences
75 Nowonro, Nowongu, Seoul 01812, Republic of Korea
Prof. T.-W. Lee
Institute of Engineering Research
Research Institute of Advanced Materials
Nano Systems Institute (NSI)
BK21 PLUS SNU Materials Division
for Educating Creative Global Leaders
Seoul National University
1 Gwanak-ro, Gwanak-gu, Seoul 08826, Republic of Korea

**ADVANCED
SCIENCE NEWS**

www.advancedsciencenews.com

**ADVANCED
FUNCTIONAL
MATERIALS**

www.afm-journal.de

Several metal-free nanomaterials containing C—C units, such as graphene QDs and carbon nanoplatelets, have been investigated as fluorescent materials. However, their weak PL efficiency and low dispersibility prevent them from being efficient as an in vivo imaging probe.[3–5] Metal-free 3D carbon nitride (C_3N_4) materials are composed of C, N alternating tri-*s*-triazine or *s*-triazine building units.[12–16] Because of suitable band structure and PL properties, 3D C_3N_4-based materials show excellent performance as visible light active photocatalysts for H_2 production and degradation of organic pollutants, and luminescent materials in chemical and biosensors.[17–20] However, self-quenching of the emitted photons in a 3D network could reduce PL efficiency. Additionally, the large dimensions and low dispersibility of these 3D materials are not appropriate for their use as bioimaging probes in a living organism.[6,7,21–24] Recently, chemical modification of 3D C_3N_4 networks and insertion of solvent molecules into interlayer galleries of the 3D network provided successful routes for producing exfoliated 2D C_3N_4-based nanoplatelets.[25–30] For example, chemical oxidation of 3D C_3N_4,[25] or attachment of a biocompatible and flexible group such as polyethylene glycol on 3D C_3N_4 provided aqueous homogeneous colloidal suspensions of 2D C_3N_4-based nanoplatelets.[26] These 2D materials were luminescent in aqueous media and showed good performance for in vitro cell imaging. However, in vivo fluorescence imaging attempts with the dispersed materials has not been successful, presumably because of low dispersion stability of hydrophobic sp^2 C—N networks. In particular, these previous 2D C_3N_4 materials have not shown sufficient PL to overcome live tissue autofluorescence, thereby not resulting in vivo fluorescence images when using them. Herein, we report a novel route to produce stable aqueous suspensions of fluorescent, thin, and 2D C_3N_4 nanoplatelets. The nanoplatelets showed excellent performance as a bioimaging probe to conduct an in vivo fluorescence imaging study, as the first case of a C_3N_4 framework.

2. Results and Discussion

2.1. Preparation and Characterization of UCN-H Powder and Suspensions

3D C_3N_4, which has been referred to as graphitic or polymeric C_3N_4, can be produced by thermal condensation of small organic precursors such as melamine, dicyandiamide, or urea.[31–34] However, the chemical structure of the basic building units and their long-range ordering in the 3D network depend on synthetic conditions such as type of precursors and gaseous conditions.[35,36] To find the best synthetic conditions for producing aqueous suspensions of C_3N_4-based materials, several 3D C_3N_4 samples were prepared while varying i) the type of precursor (melamine, dicyandiamide, or urea) and ii) the gaseous medium (air or N_2) (see Supporting Information for experimental details). However, based on our experiments, not all attempts produced promising results for the production of stable aqueous suspensions and in vivo imaging performance. Among the common precursors, it was suggested that the use of urea produced 3D C_3N_4 materials with more porous morphology and larger surface area,[37,38] and our experiments,

indeed, confirmed this (Table S1, Supporting Information). During the polycondensation of urea, CO_2 gas is generated because the urea molecules contain oxygen atoms.[37,38] This gas evolution hampers growth of the basic building units into large crystals, decreasing grain size. Inspired by this concept, we used humidified air as a gas source during the polycondensation of urea.

To maximize the effect of the water treatment, urea powder was first mixed with purified water, then the mixture was heated at 550 °C in a furnace with a flow of a humidified air gas for 4 h (**Figure 1**a, Figures S1 and S2, Supporting Information). The mixed gas was generated by bubbling air through water. The resulting powder was further heated at 550 °C with an N_2 flow for 4 h, producing a pale yellow powder (urea-driven C_3N_4 with H_2O treatment, UCN-H). Scanning electron microscopy (SEM) images of the UCN-H powder show a porous structure (Figure S3, Supporting Information) and its Brunauer–Emmett–Teller (BET) surface area was as high as 149 m^2 g^{-1}. This value was 375% higher than that (40 m^2 g^{-1}) of urea-driven C_3N_4 (UCN) powder, which was separately produced without the water/humidified air treatment.

X-ray diffraction (XRD) analysis, which is a common fingerprint for understanding the in-plane structure of C_3N_4-based materials,[13,17,39,40] showed interesting structural features of the UCN-H. The patterns of both UCN-H and UCN powders, which were in nonexfoliated state, exhibited peaks at 13.1° and 27.4° (Figure 1b), corresponding to the in-planar structural packing motif of tri-*s*-triazine and the inter-planar distance between C_3N_4 layers, respectively.[32,33] In contrast, the peak at 13.1° was much weaker for the UCN powder. This suggests that the in-planar ordering of the tri-*s*-triazine building unit was more crystalline in the UCN-H powder than the UCN powder when they are in the nonexfoliated state. The chemical structure of the materials was further analyzed with solid state nuclear magnetic resonance (SSNMR) spectroscopy using UCN and UCN-H powder samples in nonexfoilated state (Figure 1c). The ^{13}C SSNMR spectrum of UCN-H showed the presence of C atoms in the inside (C_i) of the C_3N_4 network and adjacent (C_e and C_b) to bridging N atoms.[14] Previous reports suggested that 3D C_3N_4 materials are composed of oligomeric C_3N_4-based units linked through H-bonding.[41] The H-bonding can be broken by thermal annealing at high temperatures (>600 °C), generating higher amounts of C_b species (Figure 1c). This indicates a decrease in grain size of the C_3N_4-based building units. Interestingly, the shoulder peak for C_b was significantly enhanced in the spectrum for UCN-H compared to that of UCN (Figure 1c).

X-ray photoelectron spectroscopy (XPS) C1*s* and N1*s* spectra of 3D and nonexfoliated UCN-H were similar to those of common C_3N_4 materials (Figure 1d, and Figure S4 and Table S2, Supporting Information).[4,39,42,43] The C1*s* spectrum showed a large peak at 288.2 eV, assignable to the N=C—N moieties of triazine units and a deconvoluted N1*s* spectrum found peaks at 398.8, 400.1, and 401.4 eV, corresponding to C=N—C groups, tertiary N atoms, and amino functional groups, respectively.[13,40] A Fourier-transform infrared (FT-IR) spectrum of the UCN-H showed characteristic peaks of C_3N_4 at 1638, 1574, 1539, 1460, and 1406 cm^{-1}, corresponding to heptazine-based repeating units (Figure 1e).[13,25,39] Additional peaks at 805, 1316, and 1236 cm^{-1} correspond to triazine rings, completely condensed C—N

ADVANCED
SCIENCE NEWS
www.advancedsciencenews.com

ADVANCED
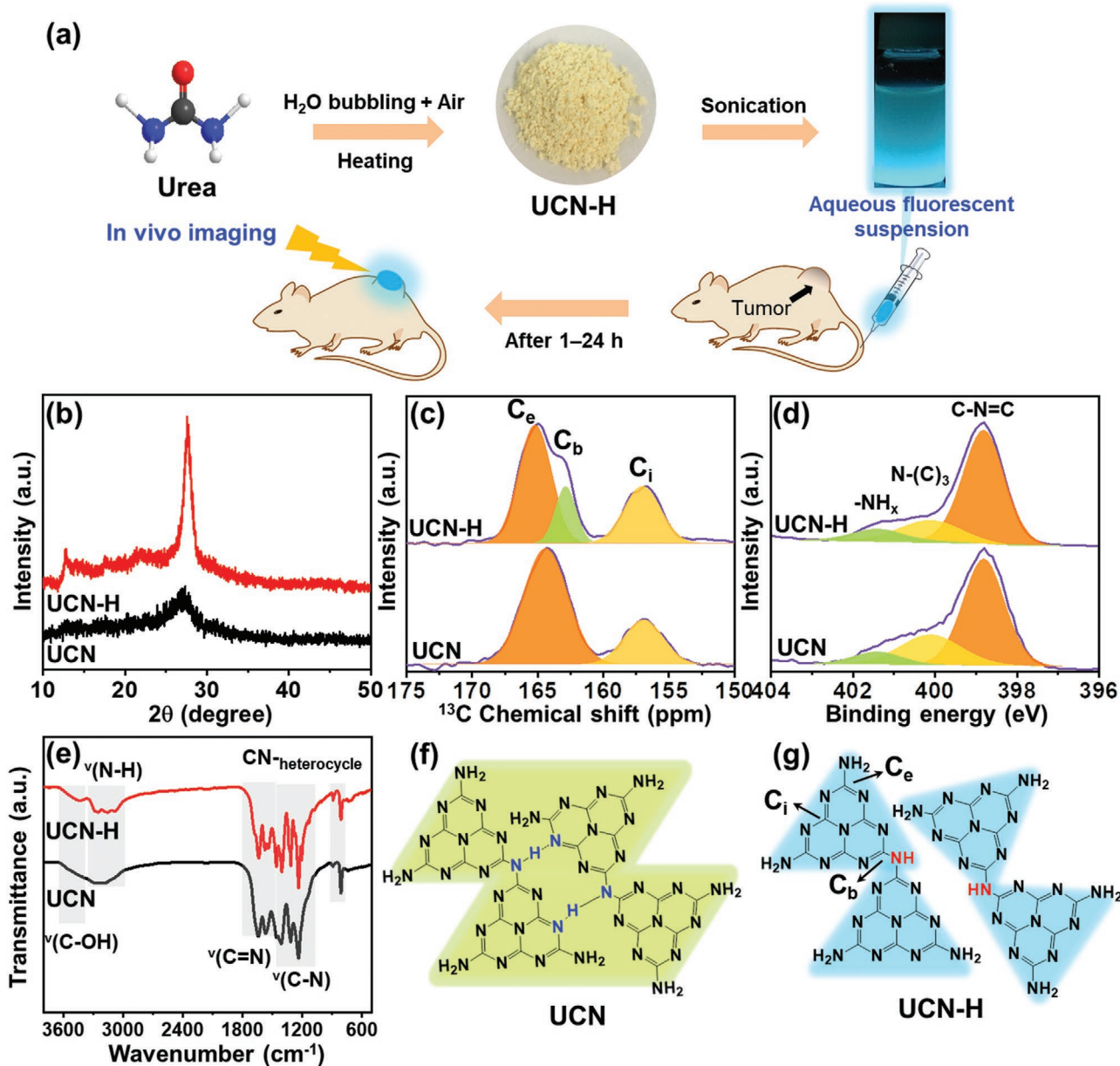FUNCTIONAL
MATERIALS
www.afm-journal.de

Figure 1. a) A diagram for the use of UCN-H as an in vivo imaging probe (a fluorescent photograph of the UCN-H dispersion with concentration of 0.5 mg mL^{-1} was taken under 365 nm UV light), chemical characterizations for UCN and UCN-H powder in nonexfoliated state b) XRD patterns, c) ^{13}C SSNMR spectra, d) deconvoluted XPS N 1s spectra, e) FT-IR spectra at full region, and f,g) chemical structures of UCN and UCN-H.

moieties, and partially condensed C−NH moieties, respectively. All these chemical characterizations confirm that the main structure of 3D UCN-H is a C, N alternating C$_3$N$_4$ network.

While partially polymerized polymeric melons or melem oligomers contain terminal amine groups (−NH$_x$), fully condensed C$_3$N$_4$ materials in principle do not contain amine groups but rather tertiary N species (N−C$_3$). Because amine groups are located at the edges of C$_3$N$_4$ layers, a smaller N−C$_3$/−NH$_x$ ratio indicates the presence of more edge structures, and in turn, the generation of a smaller grain size.[36] Recent SSNMR measurements with isotope-labeled C$_3$N$_4$ materials also supports the generation of small grain sizes with six or more melem

oligomer subunits in urea-based materials.[14] Our calculation of the N−C$_3$/−NH$_x$ ratio using XPS deconvolution showed a smaller ratio (2.2) for the UCN-H than the UCN (3.5), implying a smaller grain size for the UCN-H (Table S3, Supporting Information). The FT-IR spectrum of the UCN-H exhibits a divided peak around 3000–3400 cm^{-1}, corresponding to −NH$_x$ stretching modes.[42,44] In contrast, UCN and C$_3$N$_4$ materials produced from melamine and dicyandiamide precursors showed small shoulders at this region (Figure 1e). These data suggest that the UCN-H contains more edge structures than other C$_3$N$_4$-based materials. The rich −NH$_x$ groups at the edges of UCN-H will improve dispersibility in water. Indeed, sonication of the UCN-H

**ADVANCED
SCIENCE NEWS**

www.advancedsciencenews.com

**ADVANCED
FUNCTIONAL
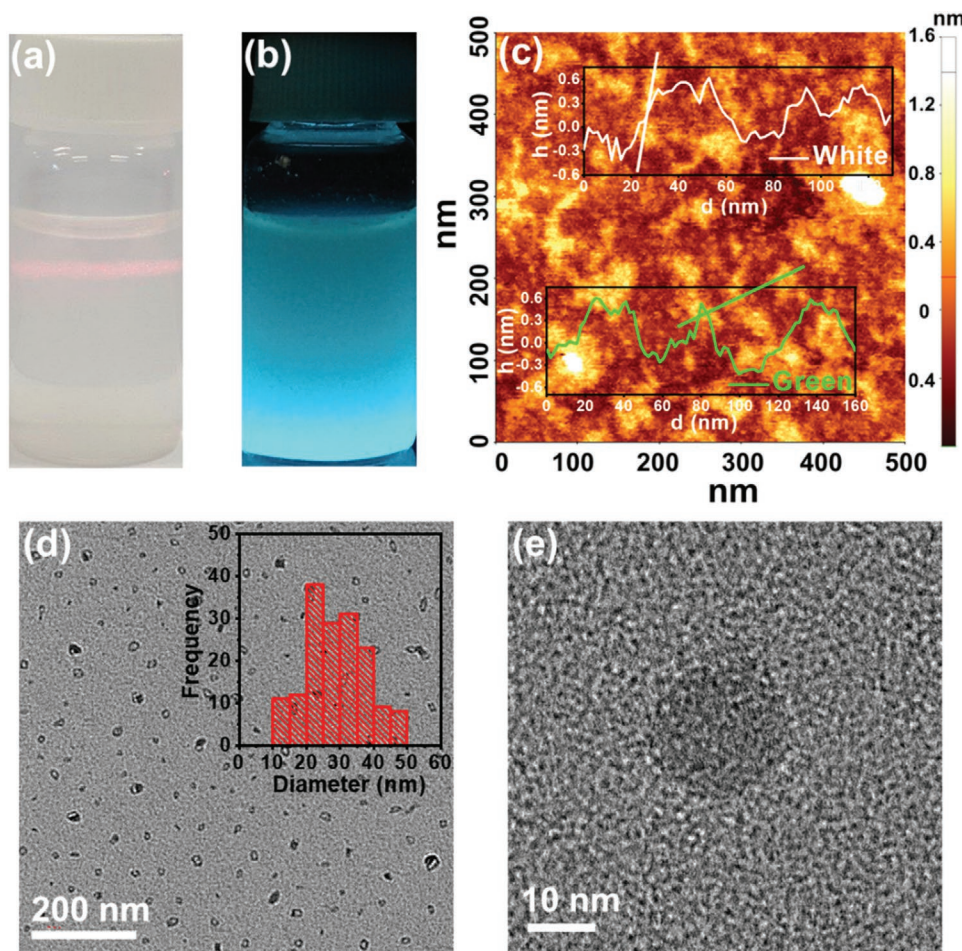MATERIALS**

www.afm-journal.de

Figure 2. Characterization of UCN-H materials. a) A photo of an aqueous colloidal suspension of 2D UCN-H with concentration of 0.5 mg mL^{-1} showing the Tyndall effect, b) a photo of the UCN-H suspension (0.5 mg mL^{-1}) showing blue luminescence upon excitation by a UV lamp, c) an AFM image of UCN-H nanoplatelets, d) a TEM images of UCN-H nanoplatelets with a distribution profile of particle size (the averaged size was 28.9 ± 8.98 nm) , and e) a TEM image of UCN-H nanoplatelet with a high magnification.

powder produced a highly stable, homogeneous colloidal suspension of 2D UCN-H nanoplatelets in water (**Figure 2**a).

Transparent, homogeneous, and fluorescent colloidal suspensions of 2D UCN-H were produced by sonication of the 3D UCN-H powder in water (Figure 2a,b). The suspensions were stable for at least several weeks without any agglomeration and show the Tyndall effect, confirming the presence of particles in the suspensions (Figure S5, Supporting Information). The UCN-H suspension had the bigger absolute value of zeta potential (−51.0 mV) than the UCN suspension (−39.4 mV) . It is indicative of the presence of more charges at the surface of UCN-H, leading the better dispersibility in water.[45] It would be attributed to the generation of amine groups at the edges of UCN-H. In fact, from the ^{13}C SSNMR, XPS, and FT-IR measurements, we showed that there exist more amine groups in UCN-H than in UCN. The presence of more amine groups at the surface of UCN-H indicates that the intra-domain H-bonding is broken and thus would enable better dispersion of UCN-H in water. The aqueous suspensions are stable under acidic, neutral, and basic conditions (pH = 5, 7, and 9, respectively) (Figure S6, Supporting Information). Particle sizes in the basic condition, which were

determined by dynamic light scattering (DLS) measurements, were bigger than those in acidic and neutral conditions. It can be explained by the presence of amine functional groups.[29] For possible applications as in vivo imaging probes, the fluorescent materials should be dispersed in phosphate buffered saline (PBS) solution. The presence of various ions, such as Na$^+$, K$^+$, and PO$_4^{3-}$ in the buffer solution, often reduces the dispersibility of materials, which are even well-dispersed in de-ionized water. Interestingly, the UCN-H was well-dispersed in the PBS solution while UCN showed poor dispersibility (Figure S7, Supporting Information). It facilitates to apply them to in vivo imaging systems. Morphological properties of the particles in the UCN-H suspensions were investigated by transmission electron microscopy (TEM) and atomic force microscopy (AFM) measurements of dried droplets of the suspensions. The TEM measurements using a carbon film grid show well-dispersed thin nanoplatelets 20–40 nm in length (Figure 2d,e). The thickness of the nanoplatelets was determined to be ≈1 nm using height profiles of AFM measurements (Figure 2c), confirming the presence of atomically thin nanoplatelets. The UCN materials were less dispersible in water (Figure S8, Supporting
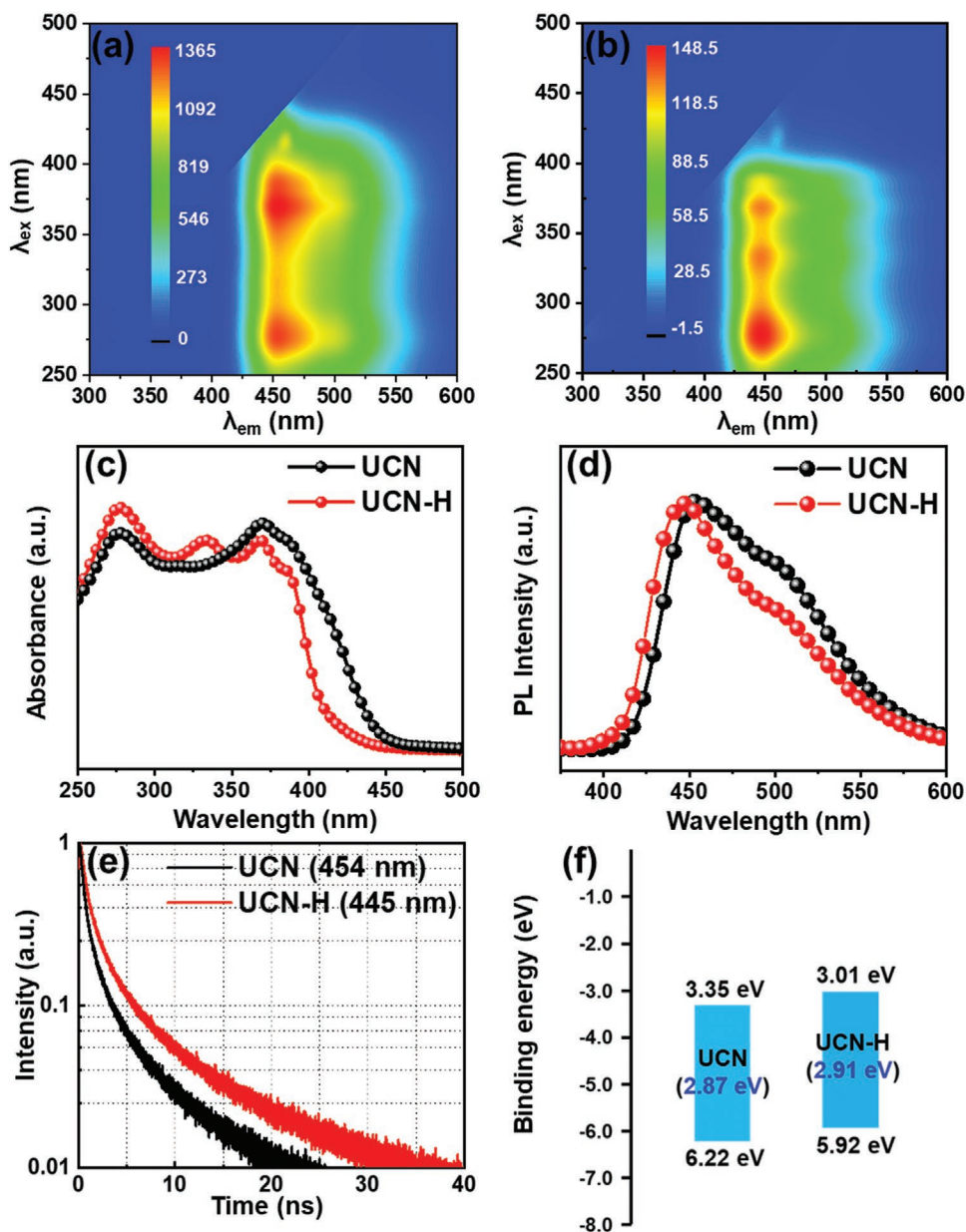
Figure 3. a,b) 2D excitation-emission spectra of a) UCN and b) UCN-H powder. c) Absorption spectral profiles of UCN (black) and UCN-H (red) extracted from the 2D excitation-emission spectrum. d) The PL spectra of UCN (black) and UCN-H (red) measured with 355 nm excitation and the PLE spectra of UCN (black) and UCN-H (red) measured at the detection wavelength of 450 nm. The absorption and PL spectra were normalized for easier comparison. e) Time-resolved PL decays of UCN and UCN-H under 393 nm excitation at the emission wavelength corresponding to the major peak (454 nm for UCN and 445 nm for UCN-H) and f) band energy diagrams of UCN and UCN-H.

Information) and TEM images of the UCN found agglomerated particles (Figure S9, Supporting Information).

2.2. Photophysical Properties of UCN-H and UCN

It is important to examine the optical properties of 2D UCN-H nanoplatelets to assess their possible applicability in bioimaging. The suspensions emit blue visible light upon excitation with a UV lamp (Figure 2b). The UV-Vis absorption spectrum of UCN-H powder shows a broad peak between 250 and 450 nm

(Figure S10, Supporting Information). The bandgap (E_g) was determined to be 2.91 eV, corresponding to blue light, from the absorption spectrum using the Kubelka-Munk function (Figure S11, Supporting Information). The valence band energy (E_v) of the UCN-H was calculated to be 5.92 eV using the ultra-violet photoelectron spectroscopy (UPS) data with an excitation energy of 21.21 eV (Figure S12, Supporting Information). The conduction band energy (E_c) is thus estimated at 3.01 eV from $E_v - E_g$. The bandgap of UCN-H was slightly bigger than that (2.87 eV) of UCN, and band energy levels of UCN were slightly lower than those of UCN-H (**Figure 3**f). After exfoliation as 2D

**ADVANCED
SCIENCE NEWS**

www.advancedsciencenews.com

**ADVANCED
FUNCTIONAL
MATERIALS**

www.afm-journal.de

UCN-H nanoplatelets in water, the absorption peak around 320 nm became significantly narrower (Figure S10, Supporting Information). This implies improved homogeneity of light-adsorbing units after exfoliation as 2D nanoplatelets.

As shown in Figure 3a,b, we measured the 2D excitation-emission spectra of the UCN and UCN-H dispersion samples, respectively, to examine the effect of the water/humidified air treatment on their emission properties. Both UCN and UCN-H samples exhibited the emission at 420–550 nm with the strongest emission at ≈450 nm. It can be seen that the shape of the PL spectrum for each sample stays the same irrespective of the excitation wavelength. Since we found that the spectral features in the excitation wavelength axis of the 2D excitation-emission spectrum is better resolved than in the raw absorption spectrum measured for each sample (Figure S13, Supporting Information), we obtained the absorption profile of each sample, as shown in Figure 3c, by integrating the 2D excitation-emission spectrum along the emission wavelength axis. In this manner, we can emphasize only the absorption features of the emitting domains. It can be seen that the absorption edge of UCN-H is blue-shifted compared with that of UCN and the absorption features of UCN-H are sharper than those of UCN. Since the lowest absorption of UCN and UCN-H corresponds to the $\pi \rightarrow \pi^*$ transition of the aromatic sp^2 C=N units, the blue shift reflects the smaller grain size of UCN-H than that of UCN,[46,47] in agreement with the results of ^{13}C NMR, XPS, and FT-IR measurements. Also, the sharper absorption features of UCN-H indicate that UCN-H nanoplatelets in dispersion are more crystalline with better-defined grain structures than UCN nanoplatelets in dispersion, which is in agreement with the XRD result of nonexfoliated powder samples.

In Figure 3d, we show the PL spectrum measured with 355 nm excitation. It can be seen that the peak of the PL spectrum of UCN-H is blue-shifted compared with that of UCN, which is in agreement with their absorption profiles. Notably, it can be seen that the ratio of the intensities of the major and the shoulder peaks is larger for UCN-H than for UCN. Since the shoulder peaks at 508 nm (for UCN) and 502 nm (for UCN-H) correspond to the emission from the intra-bandgap traps,[48,49] the difference in the ratio of major-to-shoulder peak intensities indicates that there exist less intra-bandgap traps in UCN-H than in UCN. According to the temporal profiles of time-resolved PL shown in Figure 3e UCN-H exhibits a slower PL decay at the emission wavelength of the major peak than UCN, with the average PL lifetimes of 9.2 ns for UCN-H and 6.8 ns for UCN.

The longer PL lifetime of UCN-H (9.2 ns) than that of UCN (6.8 ns) is beneficial for utilization of its PL properties (Table S4, Supporting Information). A previous report suggested that the τ_3 corresponds to the inter-planar migration along the π-stacking direction.[50] The much longer τ_3 of UCN-H compared to that of UCN can be attributed to the better crystallinity of UCN-H along the π-stacking direction. This leads to easier migration of charge carriers between C_3N_4 layers, resulting in a longer τ_3.

2.3. Cell Viability and In Vitro Imaging Study of UCN-H Nanoplatelets

Considering the beneficial properties of UCN-H suspensions, such as excellent dispersibility in water, high stability of the suspensions, and long PL lifetimes, we applied them as optical/fluorescence imaging probes in vitro as well as in vivo and investigated their biocompatibility and cytotoxicity. For evaluation of the biocompatibility of the thin UCN-H nanoplatelets, we measured the amount of viable cells after 24 and 48 h of incubation at varying concentrations (0, 25, 50, or 100 µg mL^{-1}) of the UCN-H nanoplatelets with MDA-MB-231 and RAW 264.7 cells using a trypan blue exclusion assay. As can be seen from **Figure 4**a, cell proliferation is barely hindered by the presence of 25 and 50 µg mL^{-1} UCN-H nanoplatelets at both 24 and 48 h incubation times. Furthermore, the cell viability of MDA-MB-231 and RAW 264.7 cells were 89.7% and 82.6%, respectively, with the highest concentration of UCN-H nanoplatelets (100 µg mL^{-1}) even after 48 h of incubation time. This result indicates that the UCN-H nanoplatelets have an excellent biocompatibility and noncytotoxicity, prompting further bioimaging study.

Using confocal fluorescence microscopy, we carried out an in vitro cell-imaging study on RAW 264.7 cells with UCN-H nanoplatelets at concentrations of 0 and 3 µg mL^{-1} and stained with DAPI. After incubation with UCN-H nanoplatelets for cell-labeling for 24 h, clear confocal fluorescent images of the RAW 264.7 cells were obtained without any cytosolic aggregation. The UCN-H, which labeled RAW 264.7 cells, maintained their normal morphology as well as cell activity at all concentrations, as shown in Figure 4b. In these confocal microscopic cell images, the bright green-emitting UCN-H nanoplatelets mainly remained in the cytoplasm after their internalization into the cell, forming continuous circles in terms of cell morphology. In particular, their favorable PL properties allowed the RAW 264.7 cells to be successfully visualized with a relatively low concentration of UCN-H nanoplatelets (3 µg mL^{-1}). Based on these cell imaging results, the UCN-H nanoplatelets were further applied as a fluorescent probe for in vivo molecular imaging.

2.4. In Vivo and Ex Vivo Imaging Study Using UCN-H

The favorable optical and biocompatible properties of the thin UCN-H nanoplatelets prompted further in vivo bioimaging studies. To evaluate any possible interference between the fluorescent signal from the nanoplatelet and live tissue autofluorescence, we performed an in vivo fluorescent imaging study using a normal mouse model subcutaneously injected with UCN-H nanoplatelets at different dosages (0, 25, 50, and 100 µg) as shown in **Figure 5**a. In the in vivo fluorescent image of the normal mouse, fluorescent signals were detected at all sites where any dose of nanoparticles was administered without any interference from live tissue autofluorescence. In particular, using only a 25 µg dose of the UCN-H nanoplatelets provided fluorescence signals on the mouse model surface.

Considering the excellent performance of the UCN-H nanoplatelets in the in vivo fluorescent optical imaging system, in vivo fluorescent imaging was further studied using tumor mice models. For this purpose, female nude mice bearing a subcutaneous MDA-MB-231 human breast adenocarcinoma on their right thigh were injected at the foot-pad with 100 µg of UCN-H nanoplatelets dispersed in PBS solution (50 µL). Then in vivo fluorescent images were obtained from the anesthetized mice at 1, 3, 6, 24, and 48 h intervals after the injection. As depicted
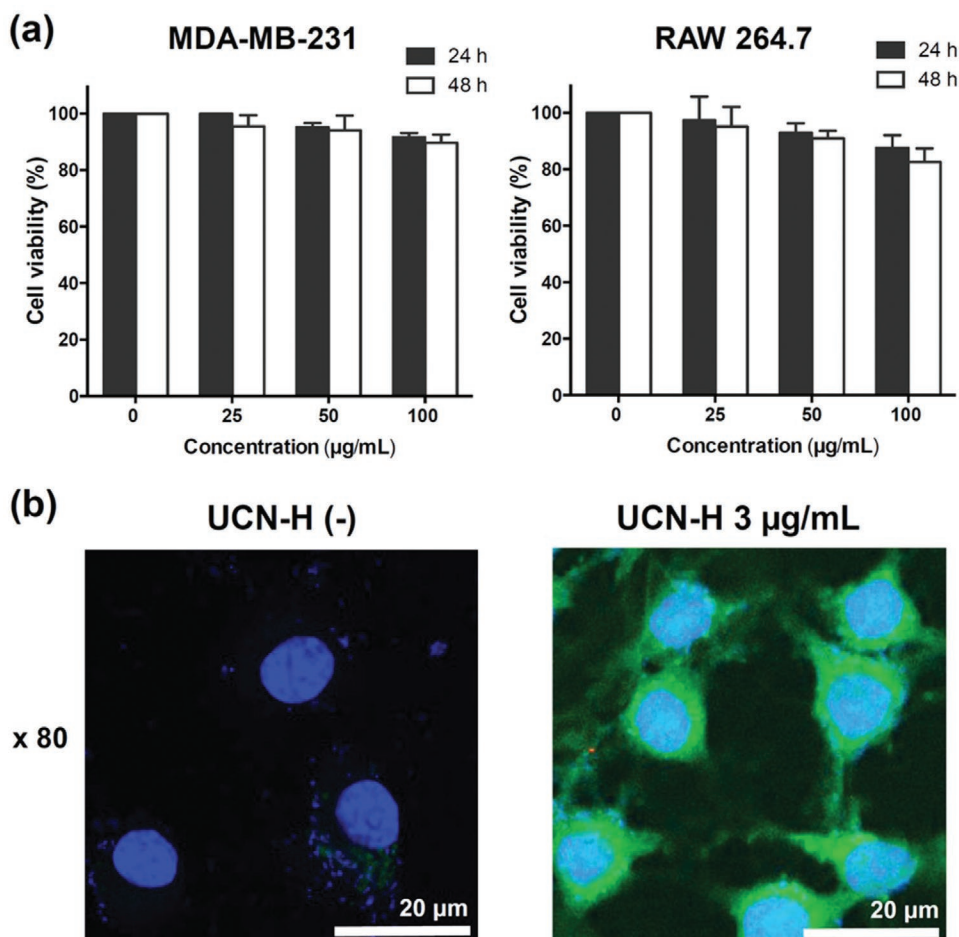
ADVANCED
SCIENCE NEWS
www.advancedsciencenews.com

ADVANCED
FUNCTIONAL
MATERIALS
www.afm-journal.de

Figure 4. In vitro study of UCN-H nanoplatelets. a) Viability of MDA-MB-231 and RAW 264.7 cells after 24 and 48 h of incubation with different concentrations of UCN-H nanoplatelets, and b) confocal fluorescence microscopic images of RAW264.7 cells after 24 h of incubation with 3 µg mL^{-1} of UCN-H or without UCN-H at 37 °C and stained with DAPI.

in Figure 5b, a persistently strong fluorescence signal was observed in the tumor region, with a low background signal from the normal tissues, at all intervals after the injection of the UCN-H nanoplatelets. The UCN nanoplatelets as a reference could not provide a fluorescence signal on the tumor lesion in the mouse model at 3 h post-injection (Figure 5c, left). In contrast, the "label-free" UCN-H nanoplatelets successfully enabled visualization of the tumor site with a high fluorescent signal intensity due to their excellent PL and PBS-dispersible properties compared with those of the UCN (Figure 5c, right). It is important to note that this in vivo optical imaging result is the first example obtained using 2D carbon-nitride nanomaterials without any labeling process.

We further carried out an ex vivo imaging study from the necropsied mice after the last fluorescent imaging scans at 48 h after injection to confirm the in vivo fluorescent imaging profile of UCN-H nanoplatelets. As shown in the ex vivo images (Figure 5d, upper row), the UCN-H nanoplatelets show high tumor-accumulation with strong fluorescence intensity of the tumor region compared with other major organs such as liver, spleen, kidney, and lymph node. Figure 5d (lower row) shows that the semi-quantitative data at 48 h post-injection were

well-correlated with the observations for the tumor and other major organs obtained from the ex vivo fluorescent imaging. The UCN-H nanoplatelets showed 5–11-fold higher uptake on the tumor region than on other major organs because the UCN-H nanoplatelets can accumulate in the tumor site by passive tumor targeting via the enhanced permeability and retention (EPR) effect.[51,52]

To further confirm the tumor-accretion of UCN-H nanoplatelets, a histological analytical study was performed using a fluorescence microscope. We clearly observed bright spots in histological tumor tissue sections from the sacrificed MDA-MB-231 tumor-bearing mouse at 48 h after injection of the UCN-H nanoplatelets (Figure 5e, center). In addition, after these tumor tissue sections were stained with DAPI, the DAPI-stained images show the location of tumor tissue nuclei (Figure 5e, left). In the merged images (Figure 5e, right), UCN-H nanoplatelets (green fluorescence) is correctly matched with DAPI stained cell nuclei (blue fluorescence) under each GFP filter and DAPI filter, indicating that the nanoplatelets were well-accumulated in the tumor cells. Consequently, these biodistribution and histology results were in agreement with results from the in vivo fluorescence imaging study.
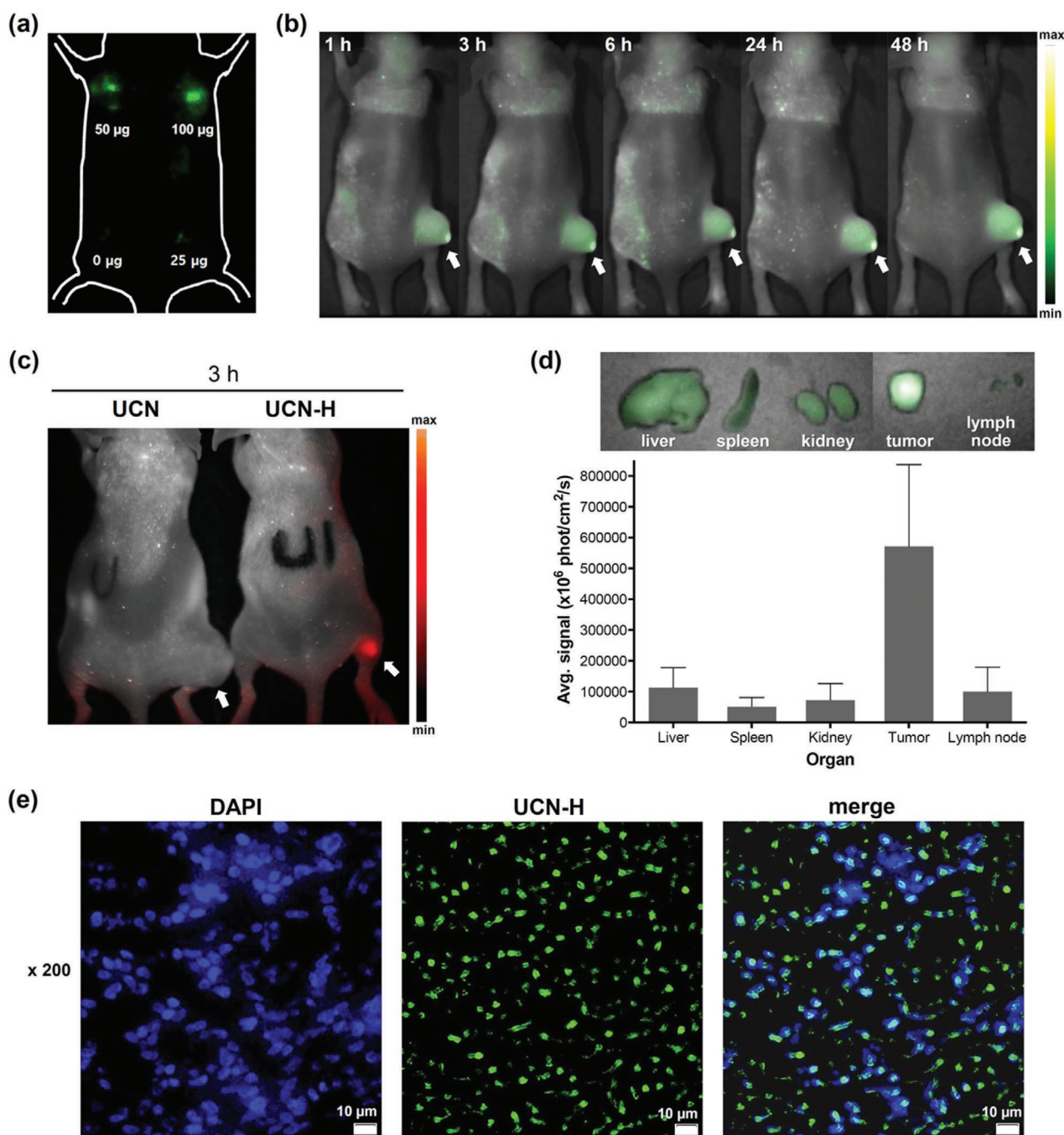
**ADVANCED
SCIENCE NEWS**

www.advancedsciencenews.com

**ADVANCED
FUNCTIONAL
MATERIALS**

www.afm-journal.de

Figure 5. In vivo and ex vivo fluorescent imaging study with UCN-H: a) In vivo fluorescent imaging of a normal mouse model subcutaneously injected with UCN-H nanoplatelets different dosages (25, 50, and 100 µg) . b) In vivo fluorescent images of MDA-MB-231 tumor-bearing mouse injected at the foot-pad with 100 µg of UCN-H nanoplatelets recorded at 1, 3, 6, 24, and 48 h after injection. c) Comparison of fluorescence imaging from UCN or UCN-H injected MDA-MB-231 tumor-bearing mouse. White arrows refer to the tumor position. d) Ex vivo fluorescent images of the major organs of MDA-MB-231 tumor-bearing mouse, 48 h after injection of UCN-H nanoplatelets, and their quantified necropsy data ($n = 5$). e) Histological analysis: fluorescent microscopic images of tumor tissue sections from the MDA-MB-231 tumor-bearing mouse 48 h after injection of UCN-H nanodots (center), the tumor tissue section images after staining with DAPI (left), and their merged images (right).

3. Conclusion

In this work, we developed a novel method to produce metal-free, biocompatible, fluorescent bioimaging probes. UCN-H powder was produced by polycondensation of urea under water/humidified air treatment. Chemical and photophysical analyses, including XPS, FT-IR, SSNMR, and XRD measurements, found that the grain size and chemical structures of basic building units of the UCN-H powder were controlled by the humidified air treatment. The grain size of C_3N_4 network in UCN-H was

**ADVANCED
SCIENCE NEWS**
www.advancedsciencenews.com

**ADVANCED
FUNCTIONAL
MATERIALS**
www.afm-journal.de

smaller than that in UCN and more amine groups were generated at edges of UCN-H than UCN. Then sonication of the material produced stable aqueous and fluorescent UCN-H suspensions. TEM measurements confirmed that the suspensions contain thin and 2D nanoplatelets. The suspensions are stable in acidic, neutral, and basic media and the excellent dispersibility was confirmed by zeta potential measurements. The PL, TR-PL, and 2D excitation-emission spectra showed that UCN-H has less-intra bandgap traps and longer PL lifetime than UCN, which will be advantageous for using them as optical bioimaging probes. The resulting noncytotoxic UCN-H nanoplatelets showed excellent performance as a biological imaging probe in in vitro as well as in vivo experiments using an animal model. In in vivo fluorescence imaging study using tumor-bearing mice, the 2D UCN-H nanoplatelets emitted a persistently strong fluorescence signal at the tumor region after their accumulation on the tumor site via the EPR effect in the absence of any interference with live tissue autofluorescence. In particular, the excellent PL and water-dispersible properties of 2D UCN-H nanoplatelets enabled the first in vivo optical imaging example using "heavy metal free" nanomaterials including 2D C_3N_4 without any labeling process. On the basis of these results, we believe that the "label-free" UCN-H nanoplatelets can play a crucial role as a novel, promising framework for molecular imaging, and this can be further extended to a variety of biomedical applications.

4. Experimental Section

Preparation of Urea-Driven C_3N_4 (UCN): Urea (5g, 99%, Sigma-Aldrich) powder was loaded into a quartz crucible and then placed in the center of a quartz tube. The quartz tube containing precursors was degassed and filled with N_2. The temperature of the tube was heated to 550 °C at a rate of 3 °C min^{-1} and then held at temperature for 4 h in a muffle furnace under an N_2 atmosphere. After cooling to room temperature, the final product (UCN) was obtained as a pale yellow powder (237 mg).

Preparation of Urea-Driven C_3N_4 Treated by H_2O (UCN-H): Urea (5 g, 99%, Sigma-Aldrich) and de-ionized water (2 mL) were mixed in a quartz crucible, which was then placed in the center of a quartz tube. During the heating process, a mixture of H_2O and air was continuously flowed through the tube by bubbling air through deionized (DI) water (130 mL) using an air pump. The humidified air was flow with a speed of 221 L/min. With the same flow speed, an average humidity in the furnace was 93% at 25 °C (the humidity at 550 °C was not able to be measured because the commercial hygrometer (Thermo-Hygrometer, SK-110TRHII, Type 1, SATO, Tokyo, Japan) could be broken at such high temperature). The temperature in the tube was raised to 550 °C at a rate of 3 °C min^{-1} then held at temperature for 4 h in a muffle furnace. The furnace was then cooled to room temperature, to produce a pale yellow powder (82 mg).

The isolated powder (400 mg) was ground with a mortar and pestle. The resulting fine powder was loaded into a quartz crucible and then placed in the center of a quartz tube. The quartz tube containing the precursor was vacuum-degassed and filled with N_2 gas. The temperature of the tube was elevated to 550 °C at a rate of 3 °C min^{-1} and then held at temperature for 4 h in a muffle furnace under N_2 atmosphere. After cooling down to room temperature, the final product (UCN-H) was obtained as a pale yellow powder (200 mg).

Preparation of Aqueous Suspensions of the 2D UCN-H Nanoplatelets: The as-prepared UCN-H powder (3 mg per 10 mL of water) was added into a vial filled with de-ionized water. The vial was then sonicated for 200 min using an ultrasonic cleaner (POWERsonic 410, Hwa-Shin Instrument Co., South Korea).

Cell Viability: The MDA-MB-231 (human breast adenocarcinoma) cells and RAW 264.7 (mouse macrophage) cells were cultured with DMEM media (Corning Inc., New York, USA) containing 10% fetal bovine serum and 1% antibiotics and maintained in a humidified incubator under 5% CO_2 at 37 °C. These cells (1×10^6 cells per 1 mL DMEM media) were prepared in a test-tube. Then UCN-H nanoplatelets were treated (0, 25, 50, and 100 μg) and shaking in a humidified incubator under 5% CO_2 at 37 °C for 1 h. After incubation, the supernatant were removed after centrifugation (250 g, 5 min) and washed twice with PBS solution. Washed cells were seeded on a 6-well plate with DMEM media and maintained in a humidified incubator under 5% CO_2 at 37 °C for 24 h or 48 h. Each time points, these cells were washed with PBS and counted using Countess II Automated Cell Counter (Invitrogen, California, USA) to distinguish dying cells and live cells.

Confocal Fluorescent Microscopy Image Study: The RAW 264.7 cells (2×10^5) were seeded on a 2-well chamber slides with DMEM media containing 10% FBS at 37 °C in a humidified atmosphere with 5% CO_2 for 24 h. Then, UCN-H nanoplatelets (0 and 3 μg mL^{-1}) were treated with DMEM media and incubated at 37 °C in a humidified atmosphere with 5% CO_2 for 24 h. The supernatant was removed after incubation and the cells were washed twice with PBS. RAW 264.7 cells labeled with UCN-H nanoplatelets were stained with ProLong Diamond Antifade Mountant with DAPI (Invitrogen, California, USA) and covered by microscope cover glass (Paul Marienfeld, Harsewinkel, Germany). Fluorescence images were acquired with a laser-scanning confocal microscope (LSM710, Carl Zeiss MicroImaging, Jena, Germany).

In Vivo and Ex Vivo Fluorescence Imaging: All animal experimental procedures were approved by the Institutional Animal Care and Use Committee (IACUC) at the Korea Institute of Radiological and Medical Sciences (KIRAMS) (IACUC no. KIRAMS 2019-0083). In order to confirm the degree of fluorescence in mice according to different doses of the UCN-H nanoplatelets (0, 25, 50, and 100 μg), each amount of UCN-H nanoplatelets was subcutaneously injected into the back muscle of mouse, and images were obtained using the Maestro II In-Vivo Imaging System (Califer Life science Inc., Massachusetts, USA) (excitation = 635 nm, emission = 700 nm). To confirm the passive tumor-targetability of UCN-H nanoplatelets, MDA-MB-231 human breast adenocarcinoma cells (1×10^7) was subcutaneously injected into the right thigh of 6-week BALB/c female nude mice, and the tumors were developed during 2 weeks approximately. The UCN-H in PBS (100 μg in 50 μL) were injected into the foot-pad of MDA-MB-231 tumor bearing mice anesthetized with 2% isoflurane in O_2. Fluorescence images were obtained at 1, 3, 6, 24, and 48 h after injection using the Maestro II In-Vivo Imaging System. During the imaging process, mice were anesthetized with 2% isoflurane in O_2. After in vivo imaging, the mice were sacrificed and their organs, including liver, spleen, kidney, tumor and lymph nodes were harvested. Fluorescence images of these major organs were acquired and their fluorescence signals were quantified using Maestro II In-Vivo Imaging System.

Histological Analysis: After the ex vivo image acquisition, tumor tissues were immediately covered with optimal cutting temperature (O.C.T) compound (Leica, Wetzlar, Germany) and frozen at −20 °C for 1 h. Serial sections were cut using a cryostat (Cryocut 1950, Leica, Wetzlar, Germany) into 10 μm thickness and placed on silane coating microslide glass (MUTO, Tokyo, Japan). Slides were washed three times with PBS and stained with ProLong Diamond Antifade Mountant with DAPI (Invitrogen, California, USA) and covered by microscope cover glass (Paul Marienfeld, Harsewinkel, Germany). Then, slides were blocked the light and dried at room temperature for 24 h and the fluorescence images were acquired by using an inverted fluorescence microscope (Olympus IX7, Olympus, Tokyo, Japan).

Supporting Information

Supporting Information is available from the Wiley Online Library or from the author.

**ADVANCED
SCIENCE NEWS**
www.advancedsciencenews.com

**ADVANCED
FUNCTIONAL
MATERIALS**
www.afm-journal.de

Conflict of Interest

The authors declare no conflict of interest.

[1] A. V. Naumova, M. Modo, A. Moore, C. E. Murry, J. A. Frank, *Nat. Biotechnol.* **2014**, *32*, 804.

[2] D. Peer, J. M. Karp, S. Hong, O. C. Farokhzad, R. Margalit, R. Langer, *Nat. Nanotechnol.* **2007**, *2*, 751.

[3] X. She, H. Xu, Y. Xu, J. Yan, J. Xia, L. Xu, Y. Song, Y. Jiang, Q. Zhang, H. Li, *J. Mater. Chem. A* **2014**, *2*, 2563.

[4] S. Yang, Y. Gong, J. Zhang, L. Zhan, L. Ma, Z. Fang, R. Vajtai, X. Wang, P. M. Ajayan, *Adv. Mater.* **2013**, *25*, 2452.

[5] X. Zhang, X. Xie, H. Wang, J. Zhang, B. Pan, Y. Xie, *J. Am. Chem. Soc.* **2013**, *135*, 18.

[6] Q. Lu, J. Deng, Y. Hou, H. Wang, H. Li, Y. Zhang, *Chem. Commun.* **2015**, *51*, 12251.

[7] T. Y. Ma, Y. Tang, S. Dai, S. Z. Qiao, *Small* **2014**, *10*, 2382.

[8] C. He, D. Liu, W. Lin, *Chem. Rev.* **2015**, *115*, 11079.

[9] A. L. Efros, J. B. Delehanty, A. L. Huston, I. L. Medintz, M. Barbic, T. D. Harris, *Nat. Nanotechnol.* **2018**, *13*, 278.

[10] K. J. McHugh, L. Jing, A. M. Behrens, S. Jayawardena, W. Tang, M. Gao, R. Langer, A. Jaklenec, *Adv. Mater.* **2018**, *30*, 1706356.

[11] A. Zebibula, N. Alifu, L. Xia, C. Sun, X. Yu, D. Xue, L. Liu, G. Li, J. Qian, *Adv. Funct. Mater.* **2018**, *28*, 1703451.

[12] Y. Wang, X. Wang, M. Antonietti, *Angew. Chem., Int. Ed.* **2012**, *51*, 68.

[13] A. Thomas, A. Fischer, F. Goettmann, M. Antonietti, J. Müller, R. Schlögl, J. M. Carlssonk, *J. Mater. Chem.* **2008**, *18*, 4893.

[14] Y. Hu, Y. Shim, J. Oh, S. Park, S. Park, Y. Ishii, *Chem. Mater.* **2017**, *29*, 5080.

[15] B. Jürgens, E. Irran, J. Senker, P. Kroll, H. Müller, W. Schnick, *J. Am. Chem. Soc.* **2003**, *125*, 10288.

[16] Q. Cao, B. Kumru, M. Antonietti, B. V. Schmidt, *Mater. Horiz.* **2020**, *7*, 762.

[17] X. Wang, K. Maeda, A. Thomas, K. Takanabe, G. Xin, J. M. Carlsson, K. Domen, M. Antonietti, *Nat. Mater.* **2009**, *8*, 76.

[18] Y. Zheng, Y. Jiao, J. Chen, J. Liu, J. Liang, A. Du, W. Zhang, Z. Zhu, S. C. Smith, M. Jaroniec, *J. Am. Chem. Soc.* **2011**, *133*, 20116.

[19] V. W. Lau, I. Moudrakovski, T. Botari, S. Weinberger, M. B. Mesch, V. Duppel, J. Senker, V. Blum, B. V. Lotsch, *Nat. Commun.* **2016**, *7*, 12165.

[20] S. An, G. Zhang, T. Wang, W. Zhang, K. Li, C. Song, J. T. Miller, S. Miao, J. Wang, X. Guo, *ACS Nano* **2018**, *12*, 9441.

[21] M. Xiang, J. Liu, N. Li, H. Tang, R. Yu, J. Jiang, *Nanoscale* **2016**, *8*, 4727.

[22] J. Sun, R. Phatake, A. Azoulay, G. Peng, C. Han, J. Barrio, J. Xu, X. Wang, M. Shalom, *Chem. - Eur. J.* **2018**, *24*, 14921.

[23] M. Yang, H. Mei, Y. Shen, K. Wu, D. Pan, S. Liu, T. Zhang, Y. Zhang, *Chem. - Eur. J.* **2019**, *25*, 10188.

[24] Y. Luo, Y. Yang, Q. Cui, R. Peng, R. Liu, Q. Cao, L. Li, *ACS Appl. Bio. Mater.* **2019**, *2*, 5127.

[25] J. Oh, R. J. Yoo, S. Y. Kim, Y. J. Lee, D. W. Kim, S. Park, *Chem. - Eur. J.* **2015**, *21*, 6241.

[26] J. K. Kim, S. Park, R. J. Yoo, H. J. Jeong, J. Oh, Y. J. Lee, S. Park, D. W. Kim, *Chem. - Eur. J.* **2018**, *24*, 3506.

[27] Y. Wang, L. Li, Y. Wei, J. Xue, H. Chen, L. Ding, J. Caro, H. Wang, *Angew. Chem., Int. Ed.* **2017**, *56*, 8974.

[28] J. Ran, W. Guo, H. Wang, B. Zhu, J. Yu, S. Qiao, *Adv. Mater.* **2018**, *30*, 1800128.

[29] B. Kumru, M. Antonietti, B. V. Schmidt, *Langmuir* **2017**, *33*, 9897.

[30] N. Karjule, R. Phatake, M. Volokh, I. Hod, M., *Small Methods* **2019**, *3*, 1900401.

[31] F. K. Kessler, Y. Zheng, D. Schwarz, C. Merschjann, W. Schnick, X. Wang, M. J. Bojdys, *Nat. Rev. Mater.* **2017**, *2*, 17030.

[32] Y. Zhang, J. Liu, G. Wu, W. Chen, *Nanoscale* **2012**, *4*, 5300.

[33] F. Dong, Z. Wang, Y. Sun, W. Ho, H. Zhang, *J. Colloid Interface Sci.* **2013**, *401*, 70.

[34] D. Wang, J. Pan, H. Li, J. Liu, Y. Wang, L. Kang, J. Yao, *J. Mater. Chem. A* **2016**, *4*, 290.

[35] J. Zhu, P. Xiao, H. Li, S. A. Carabineiro, *ACS Appl. Mater. Interfaces* **2014**, *6*, 16449.

[36] J. Oh, J. M. Lee, Y. Yoo, J. Kim, S. Hwang, S. Park, *Appl. Catal., B* **2017**, *218*, 349.

[37] X. Song, Y. Hu, M. Zheng, C. Wei, *Appl. Catal., B* **2016**, *182*, 587.

[38] W. Ong, L. Tan, S. Chai, S. Yong, *Chem. Commun.* **2015**, *51*, 858.

[39] Y. Kang, Y. Yang, L. Yin, X. Kang, L. Wang, G. Liu, H. Cheng, *Adv. Mater.* **2016**, *28*, 6471.

[40] Y. Kang, Y. Yang, L. Yin, X. Kang, G. Liu, H. Cheng, *Adv. Mater.* **2015**, *27*, 4572.

[41] D. B. Nimbalkar, M. Stas, S. Hou, S. Ke, J. Wu, *ACS Appl. Mater. Interfaces* **2019**, *11*, 19087.

[42] J. Liu, T. Zhang, Z. Wang, G. Dawson, W. Chen, *J. Mater. Chem.* **2011**, *21*, 14398.

[43] V. W. Lau, M. B. Mesch, V. Duppel, V. Blum, J. Senker, B. V. Lotsch, *J. Am. Chem. Soc.* **2015**, *137*, 1064.

[44] J. Zhang, G. Zhang, X. Chen, S. Lin, L. Möhlmann, G. Dołega, G. Lipner, M. Antonietti, S. Blechert, X. Wang, *Angew. Chem., Int. Ed.* **2012**, *51*, 3183.

[45] B. Zhu, P. Xia, W. Ho, J. Yu, *Appl. Surf. Sci.* **2015**, *344*, 188.

[46] Y. Chen, B. Wang, S. Lin, Y. Zhang, X. Wang, *J. Phys. Chem. C* **2014**, *118*, 29981.

[47] G. Zhang, G. Li, T. Heil, S. Zafeiratos, F. Lai, A. Savateev, M. Antonietti, X. Wang, *Angew. Chem., Int. Ed.* **2019**, *58*, 3433.

[48] Z. Zhou, Y. Zhang, Y. Shen, S. Liu, Y. Zhang, *Chem. Soc. Rev.* **2018**, *47*, 2298.

[49] L. Meng, E. V. Ushakova, Z. Zhou, E. Liu, D. Li, D. Zhou, Z. Tan, S. Qu, A. Rogach, *Mater. Chem. Front.* **2020**, *4*, 517.

[50] H. Wang, H. Zhou, P. Li, X. Tan, Y. Liu, W. Hu, J. Ye, T. Yu, *J. Phys. Chem. C* **2018**, *122*, 17261.

[51] S. B. Lee, H. L. Kim, H. Jeong, S. T. Lim, M. Sohn, D. W. Kim, *Angew. Chem., Int. Ed.* **2013**, *52*, 10549.

[52] L. Y. Chou, K. Ming, W. C. Chan, *Chem. Soc. Rev.* **2011**, *40*, 233.